

# Equilibrium reconstruction in the START tokamak

L.C. Appel, M.K. Bevir, M.J. Walsh\*

Euratom/UKAEA Fusion Association, Culham Science Centre, Abingdon, Oxfordshire

\* Walsh Scientific Limited, Culham Science Centre, Abingdon, Oxfordshire

United Kingdom

**Abstract.** The computation of magnetic equilibria in the START spherical tokamak is more difficult than those in more conventional large aspect ratio tokamaks. This difficulty arises partly as a result of the use of induction compression to generate high current plasma, as this precludes the positioning of magnetic diagnostics close to the outboard side of the plasma. In addition, the effect of a conducting wall with a high, but finite, conductivity must be included. A method is presented for obtaining plasma equilibrium reconstructions based on the EFIT code. New constraints are used to relate isoflux surface locations deduced from radial profile measurements of electron temperature. A model of flux diffusion through the vessel wall is developed. It is shown that neglecting flux diffusion in the vessel wall can lead to a significant underestimate in the calculation of the plasma  $\beta_t$ . Using a relatively sparse set of magnetic signals,  $\beta_t$  can be obtained to within a fractional error of  $\pm 10\%$ . Using constraints to relate isoflux surface locations, the principle involved in determining the internal  $q$  profile is demonstrated.

## 1. Introduction

A knowledge of the magnetic configuration satisfying equilibrium force balance is an essential starting point for a detailed assessment of plasma performance in a tokamak. The governing equation is usually taken to be the Grad–Shafranov equation [1–12], although extensions to this equation to take account of plasma pressure anisotropy and bulk plasma rotation have also been considered [13–15]. Constraints on determining experimental equilibria are provided by a set of magnetic field detectors and flux loops arranged around the vessel, possibly interpolated to yield continuous functions of both poloidal flux  $\psi_p$  and its normal derivative  $\mathbf{n} \cdot \nabla \psi_p$  around the plasma. In these terms, the problem consists of solving an elliptic equation subject to Cauchy boundary conditions and is ill-posed, i.e. small perturbations in the boundary propagate to produce large changes in the solution a short distance from the measuring contour (Ref. [16], p. 702).

The ill-posed nature of the problem can be overcome by restricting the choice of the source functions (Ref. [16], p. 1276). A common practice is to define the plasma functions as polynomial functions of  $\psi_p$ , with coefficients to be determined during the reconstruction process. With the plasma current distribution represented by sufficiently few degrees of freedom, it is possible to design a magnetic reconstruction algorithm which is robust yet accurate. The

problem is that the class of permissible current profiles may be far from the actual magnetic configuration and one must seek a compromise between achieving a robust algorithm and not overly restricting the permissible class of current profiles.

This article reports on work carried out to reconstruct magnetic equilibria in the START spherical tokamak. The reconstructions used the EFIT code [5], which has been employed extensively for many other tokamak experiments, including DIII-D [17], JET [18] and more recently the COMPASS-D and START tokamaks. There are two distinct features of START that complicate attempts to carry out equilibrium reconstructions. The first arises from the use of induction–compression [19] to generate high performance plasmas at low aspect ratio, which precludes positioning magnetic diagnostics close to the outboard side of the plasma. The second arises from the presence of a conducting wall with high, but finite, conductivity. In conventional tokamaks the value of  $\beta_p + l_i/2$  can be determined directly from the magnetic signals without invoking force balance [3, 13, 20]; however, lack of magnetic measurements on the outboard side of the plasma means that this procedure is not satisfactory in START. This article discusses how these complications have been overcome by the implementation of a model for flux diffusion into the vessel and by the use of constraints to fix the locations of isopoloidal flux surfaces.

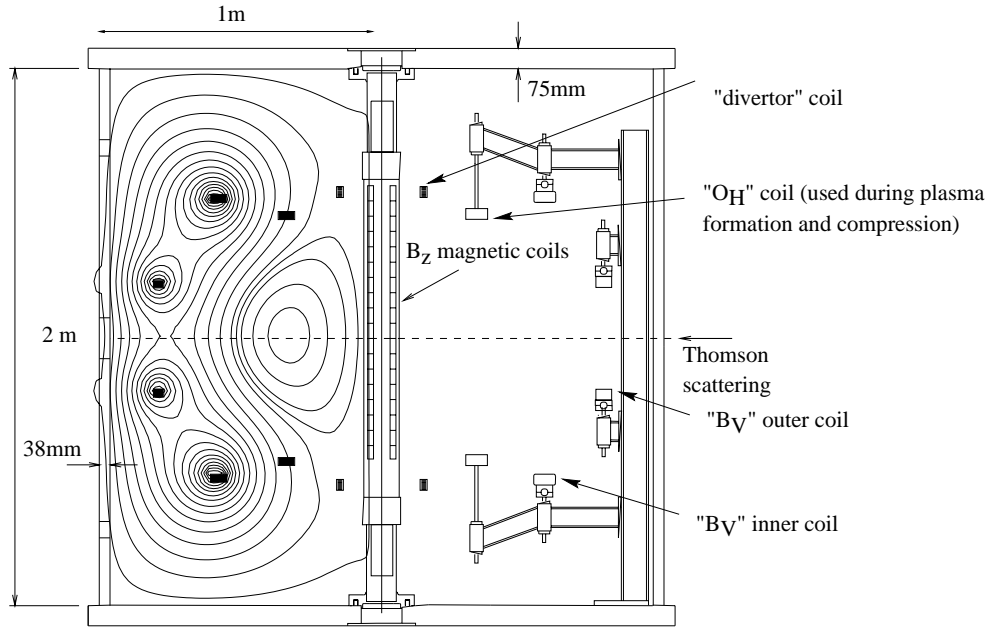


**Figure 1.** Location of START coils and diagnostics.

Figure 1 shows a cross-section of START. The plasma forms inside a vacuum tank made of aluminium alloy with vertical walls 3.8 cm thick and the two end walls 7.5 cm thick. The poloidal field coils are situated within the tank. The outer two pairs, referred to later as  $B_V$  coils, produce the dominant vertical field. The inner coil pair is for the formation of divertor plasma configurations and the remaining coil pair, referred to later as  $O_H$  coils, is used during plasma formation prior to compression. An array of 46 discrete magnetic coils measuring vertical magnetic field is located on the central solenoid, and this is screened by a thin central stainless steel tube 3 mm thick and a graphite limiter with an outer diameter of 130 mm. Rogowski coils measure the current in the poloidal field coils, and the plasma current is obtained by subtracting these signals from that of a Rogowski coil located on a poloidal plane on the inner wall of the vessel and centre column. The electron temperature and density profiles  $T_e$  and  $n_e$ , respectively, are measured with a multipoint Thomson scattering system along the horizontal midplane [21]. The system is calibrated using an HCN interferometer with a radial chord on the midplane, inwardly directed and reflected off the centre column. Ion temperatures are obtained from charge exchange spectra [22]. In addition there are two soft X ray diode arrays with horizontal and vertical views to provide information on the radius of the  $q = 1$  surface when the discharge is sawtoothing (here  $q$  is the safety factor).

In the following section we summarize the EFIT algorithm and describe a new constraint to equalize poloidal flux at pairs of user defined locations. In Section 3, a model is developed to predict flux diffusion through the START vessel wall. Finally, in Section 4, the method of obtaining equilibrium reconstructions is described, with several illustrative examples.

## 2. The EFIT algorithm

The EFIT code solves the equation for equilibrium force balance, the Grad–Shafranov equation, subject to multiple constraints that may be expressed in a large variety of ways (e.g., there are constraints based on any of the experimental signals and on the central  $q$  value). Mathematically, the Grad–Shafranov equation can be written in cylindrical co-ordinates  $(R, \phi, Z)$  as

$$\Delta^* \psi_p = -\mu_0 R J_\phi(R, Z) \quad (1)$$

where

$$\Delta^* = R \frac{\partial}{\partial R} \left( \frac{1}{R} \frac{\partial}{\partial R} \right) + \frac{\partial^2}{\partial Z^2} \quad (2)$$

and  $J_\phi(R, Z)$  is the toroidal current density which, within the plasma, can be written in terms of the flux functions  $p(\psi_p)$  and  $f(\psi_p)$  (respectively, the plasma pressure and  $RB_\phi$ ):

$$J_\phi(R, Z)^{pl} = R p' + \frac{1}{\mu_0 R} f f' \quad (3)$$

in which ' denotes  $\partial/\partial\psi_p$ . It is useful to note that  $\psi_p = RA_\phi$ , where  $A_\phi$  is the toroidal component of magnetic vector potential; the units of  $\psi_p$  are Wb/rad. The current in the poloidal field coils is represented as a set of coefficients  $I_i^{pf}$ ,  $i = 1, \dots, N_c$ . The current in the plasma is expressed as

$$J_\phi(R, Z)^{pl} = R \sum_{i=1}^{N_\alpha} \alpha_i c_i(\psi_p) + \frac{1}{\mu_0 R} \sum_{i=1}^{N_\gamma} \gamma_i d_i(\psi_p) \quad (4)$$

where  $c_i(\psi_p)$ ,  $i = 1, \dots, N_\alpha$ , and  $d_i(\psi_p)$ ,  $i = 1, \dots, N_\gamma$ , are basis functions specified at run time from a choice that currently includes polynomial functions and tension splines [23].

Equation (1) is solved iteratively, using the previous solution for  $\psi_p$  to update Eq. (2). A finite difference scheme is used to obtain the contribution of the plasma current using a regular grid consisting of  $N_p$  cells, each of area  $\delta A$ . To enhance numerical accuracy, contributions from the poloidal field coil currents are obtained using precomputed Green's functions. Interleaved between each iteration, EFIT computes updated values of the coefficients,  $\alpha_i$  ( $i = 1, \dots, N_\alpha$ ),  $\gamma_i$  ( $i = 1, \dots, N_\gamma$ ) and  $I_i^{pf}$  ( $i = 1, \dots, N_c$ ) (using the field solution of the previous iteration) to provide a best fit to the user imposed constraints. The constraints are expressed in linearized form, the representation for the  $k$ th constraint being

$$a_P^k = a_0^k + \sum_{i=1}^{N_\alpha} \frac{\partial a^k}{\partial \alpha_i} \alpha_i + \sum_{i=1}^{N_\gamma} \frac{\partial a^k}{\partial \gamma_i} \gamma_i + \sum_{i=1}^{N_c} \frac{\partial a^k}{\partial I_i^{pf}} I_i^{pf} \quad (5)$$

where  $a_P^k$  is the value of the constraint as computed by EFIT. The  $k$ th constraint equation is obtained by equating  $a_P^k$  with the user-defined target value  $a_M^k$ ,

$$\sum_{i=1}^{N_\alpha} \frac{\partial a^k}{\partial \alpha_i} \alpha_i + \sum_{i=1}^{N_\gamma} \frac{\partial a^k}{\partial \gamma_i} \gamma_i + \sum_{i=1}^{N_c} \frac{\partial a^k}{\partial I_i^{pf}} I_i^{pf} = a_M^k - a_0^k. \quad (6)$$

The assembled system of equations, weighted to reflect the accuracy of the data, is solved using the singular value decomposition method [24].

In addition to the constraints already existing in EFIT, a new constraint has been implemented enabling the poloidal flux values at one or more pairs of user-defined locations  $\mathbf{X}_{M_1}$  and  $\mathbf{X}_{M_2}$  to be equated. Writing the constraint  $a = \psi_p(\mathbf{X}_{M_1}) - \psi_p(\mathbf{X}_{M_2})$ , expressions for the coefficients of the above equations are

$$a_0 = 0 \quad (7)$$

$$\frac{\partial a}{\partial I_i^{pf}} = \frac{\partial \psi(\mathbf{X}_{M_1})}{\partial I_i^{pf}} - \frac{\partial \psi(\mathbf{X}_{M_2})}{\partial I_i^{pf}} \quad (8)$$

$$\begin{aligned} \frac{\partial a}{\partial \alpha_i} &= \sum_{j=1}^{N_p} R_j c_i(\psi_p(\mathbf{X}_j)) \delta A \\ &\times \left( \frac{\partial \psi(\mathbf{X}_{M_1})}{\partial I(\mathbf{X}_j)} - \frac{\partial \psi(\mathbf{X}_{M_2})}{\partial I(\mathbf{X}_j)} \right) \end{aligned} \quad (9)$$

$$\begin{aligned} \frac{\partial a}{\partial \gamma_i} &= \sum_{j=1}^{N_p} \frac{d_i(\psi_p(\mathbf{X}_j)) \delta A}{\mu_0 R_j} \\ &\times \left( \frac{\partial \psi(\mathbf{X}_{M_1})}{\partial I(\mathbf{X}_j)} - \frac{\partial \psi(\mathbf{X}_{M_2})}{\partial I(\mathbf{X}_j)} \right). \end{aligned} \quad (10)$$

Note that  $\partial\psi(\mathbf{X}_i)/\partial I(\mathbf{X}_j)$  is the poloidal flux at  $\mathbf{X}_i$  due to a unit toroidal current at  $\mathbf{X}_j$ .

### 3. Flux diffusion through the START vessel wall

Over the duration of a START discharge, typically 20–25 ms for a 'high performance' discharge ( $I_p > 200$  kA), the vessel wall acts as an imperfect flux conserver with a small but measurable flux ( $\approx 8$  mWb) diffusing through it. In the absence of sufficient magnetic diagnostics to quantify the induced eddy currents — START had no detectors to measure components of  $B$  or  $\psi_p$  on the outboard side of the plasma — a model has been developed to predict flux penetration through the wall.

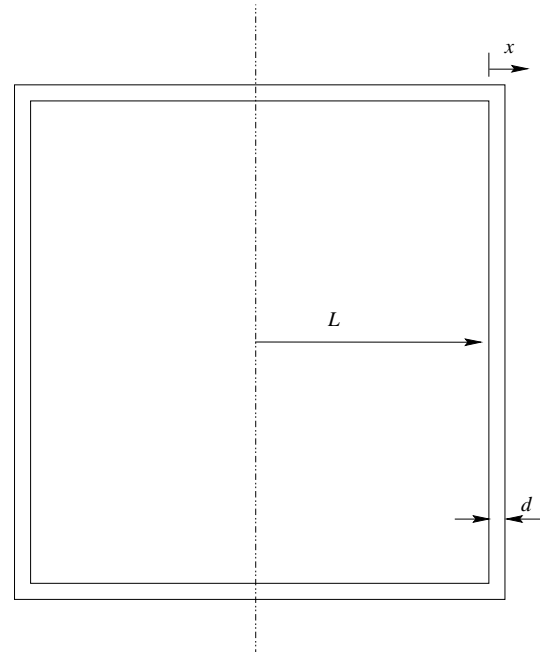


**Figure 2.** Schematic view of the START vessel showing the parameters used to describe flux diffusion through the vessel wall.

The equation for poloidal flux evolution in the START vessel (assumed to be axisymmetric and homogeneous) is

$$\nabla^2 \psi_p = \mu\sigma \frac{\partial \psi_p}{\partial t} \quad (11)$$

where  $\mu$  is magnetic permeability and  $\sigma$  is the vessel conductivity. Considering only the diffusion of flux normal to the wall, the equation reduces to

$$\frac{\partial^2 \psi_p}{\partial x^2} = \mu\sigma \frac{\partial \psi_p}{\partial t} \quad (12)$$

where, as indicated in Fig. 2,  $x$  is the perpendicular distance from the inner surface of the wall, and it is assumed that  $d \ll L$  ( $d$  is wall thickness and  $L$  is global dimension).

In developing a model for START, the tangential magnetic field  $B(t)$  at the inner wall surface is taken to be a known function of time. The behaviour of the diffusing flux is most clearly understood by examining the particular situation in which, at  $t = 0$ , a constant radial flux gradient (tangential field),  $G = \partial\psi_p/\partial x = RB(t)$ , is applied on the inner wall of the vessel ( $x = 0$ ). Initially, flux diffuses into the wall unaffected by the presence of the outer boundary. The variation of flux can be expressed (Ref. [25], p. 75) as

$$\psi_p(x, t) = 2G \left[ \sqrt{\frac{t}{\pi\mu\sigma}} \exp\left(-\frac{x^2\mu\sigma}{4t}\right) - \frac{x}{2} \operatorname{erfc}\left(\frac{x}{2}\sqrt{\frac{\mu\sigma}{t}}\right) \right] \quad (13)$$

where  $x$  is now the distance from the surface of the inner wall. A useful measure of flux penetration is the effective skin depth  $\delta$ , defined as the depth at which  $\psi_p = 0$ , assuming the poloidal flux decreases linearly from the inner wall with gradient  $G$ , and with  $\psi_p(x = 0)$  given by

$$\delta = \sqrt{\frac{4t}{\pi\mu\sigma}}. \quad (14)$$

This expression is similar to the more usual definition of skin depth defined for a field oscillating sinusoidally at angular frequency  $\omega$  [26],

$$\delta = \sqrt{2/\mu\omega\sigma}. \quad (15)$$

For  $t \gtrsim \mu\sigma d^2$ , the flux will have diffused to the outer boundary ( $d \approx \delta$ ) and Eq. (13) becomes invalid. Assuming that  $\partial\psi_p/\partial x$  at  $x = d$  is zero, so that the field at the external wall is zero, the poloidal flux is (Ref. [25], p. 112)

$$\psi_p(x, t) = \frac{Gt}{\mu\sigma d} + Gd \left[ \frac{3(d-x)^2 - d^2}{6d^2} \right] \quad (Cont.)$$

$$- \frac{2}{\pi^2} \sum_{n=1}^{\infty} \frac{(-1)^n}{n^2} \exp\left(\frac{-n^2\pi^2 t}{\mu\sigma d^2}\right) \cos \frac{n\pi(d-x)}{d} \quad (16)$$

An upper limit  $t_L$  for the applicability of this assumption can be found as follows. For very long times, the flux difference across the wall is insignificant, and the flux on the outer and inner surfaces is approximately the same, given by the first term of Eq. (16),

$$\psi_p = \frac{Gt_L}{\mu\sigma d}. \quad (17)$$

The radial flux gradient is  $G \approx \psi_p/L$ , yielding

$$t_L = \mu\sigma dL. \quad (18)$$

An estimate of  $t_L$  for the START wall using  $\sigma = 1.85 \times 10^7 \Omega^{-1} \text{ m}^{-1}$ ,  $\mu = 4\pi \times 10^{-7}$ ,  $d = 5 \text{ cm}$ ,  $L = 1 \text{ m}$  gives  $t_L \approx 1 \text{ s}$ , considerably larger than the START discharge time ( $\approx 20 \text{ ms}$ ), and hence Eq. (16) is applicable for START conditions.

The toroidal current density within the vessel wall can be expressed as

$$J_{wall}(x, t) = \frac{\sigma}{\mu R} \frac{\partial \psi_p(x, t)}{\partial t}. \quad (19)$$

The evolution of poloidal flux for an arbitrary time variation of tangential magnetic field incident on the inner wall can be obtained by first decomposing  $G(t)$  into a sum of Heaviside functions,

$$G(t) = \sum_{n=1}^m H(t - t_n) G_n. \quad (20)$$

The poloidal flux is then

$$\psi_{p[total]}(x, t) = \sum_{n=1}^m \psi_p(x, t - t_n) G_n H(t - t_n) \quad (21)$$

where  $\psi_p$  is obtained from Eq. (16). In the appendix some simple formulas for the flux and the effective skin depth are given which are valid for short and long timescales.

## 4. Implementation of EFIT for START

The external magnetic signals provide a starting point for all equilibrium calculations. Figure 1 shows the location of the 46 magnetic detectors on the centre column measuring the vertical magnetic field. Currents flowing in the poloidal field coils and

induced in their conductive metal casings are measured by Rogowski coils. In addition, there is a full Rogowski coil for measuring the plasma current and a diamagnetic loop. The two arrays of SXR diodes are available to provide the location of the sawtooth inversion radius, likely to be close to the  $q = 1$  surface, and the magnetic axis (assumed to be at the radius of peak emission). Measurements of  $T_e$  and  $n_e$  are obtained from Thomson scattering at 29 radial locations across the midplane at a single time point in each discharge. By assuming high parallel electron heat conduction, the radial profile of  $T_e$  can be used as relational constraints on flux surfaces inboard and outboard of the magnetic axis. To facilitate this, a new constraint to equalize poloidal flux values, described in Section 2, has been implemented in EFIT. Measurements of  $T_e$ ,  $n_e$  and thermal ion temperature  $T_i$  from charge exchange measurements provide the kinetic thermal pressure. The fast ion component can be computed using the Monte Carlo particle tracking code LOCUST [27].

In setting up EFIT to carry out reconstructions on START, the vacuum vessel is divided into 148 discrete elements, which can each carry a uniform current. On the inner surface of each element a virtual flux loop is defined to control the poloidal flux values on the inner surface of the vacuum vessel. To obtain an equilibrium reconstruction, EFIT is run in two stages. In the first stage, the vessel is treated as a perfect flux conserver by constraining the flux on the vessel wall to zero. EFIT runs are performed over the duration of the discharge and the time variation of the tangential magnetic field computed at each of the virtual vessel flux loop locations. Using these values, the poloidal flux at each of the flux loop locations is computed from Eq. (21). EFIT is then run for a second time, fitting to the updated poloidal flux values on the vessel wall. Although the poloidal flux at the wall could, in principle, be computed again, further iterations were found to be unnecessary.

#### 4.1. Calculations in the absence of plasma

To verify the wall model, the procedure outlined in Section 3 was used to reconstruct discharge 35345 with typical externally driven current waveforms, but without a conducting plasma. A series of runs was carried out with a range of wall conductivities in which the central magnetic detectors were not used as constraints. Figure 3 shows the time evolution of measured and predicted fields for the midplane magnetic detector on the centre tube. With zero flux pen-

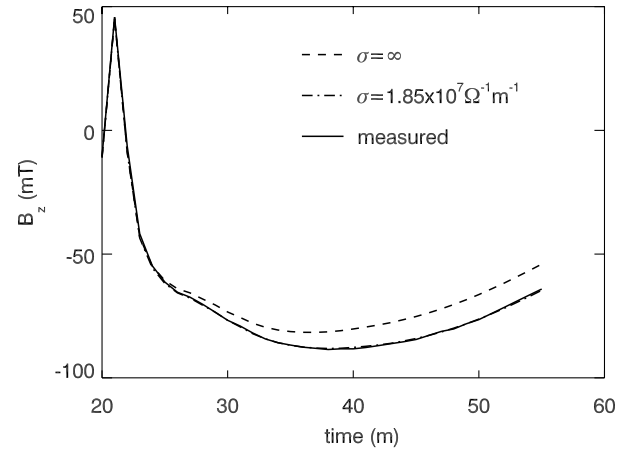


**Figure 3.** Time evolution of measured and predicted  $B_z$  signals on the inboard midplane for discharge 35345, for the perfectly conducting and resistive vessel.

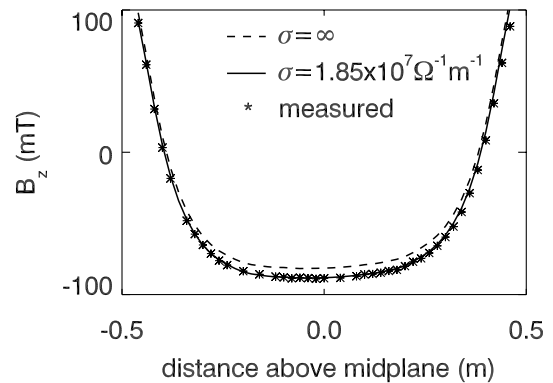


**Figure 4.** Measured and predicted  $B_z$  signals at  $t = 40$  ms for discharge 35345.

etration into the wall, the predicted magnetic field is  $\sim 15\%$  less than that measured at  $t = 40$  ms, close to when peak plasma performance would be expected. Results for other magnetic detectors are shown in Fig. 4 for  $t = 40$  ms, and are similar. Using a conductivity  $\sigma$  of  $1.85 \times 10^7 \Omega^{-1} \text{m}^{-1}$  gives a good match (to better than 1% for the central detectors). This value of  $\sigma$  will be used for the results presented later.

Figure 5 shows the evolution of the toroidal current within the vessel wall versus the distance from the inner wall at the midplane predicted from Eqs (19) and (21). The poloidal field induction currents are applied at 21 ms, causing an induced current to appear instantaneously on the inner surface of the vessel. The current immediately begins to diffuse outwards, reaching the outer vessel edge by 26 ms. The current on the inner wall continues to increase at a slower rate until  $t = 34$  ms in response to changing currents in the plasma compression coils. The figure

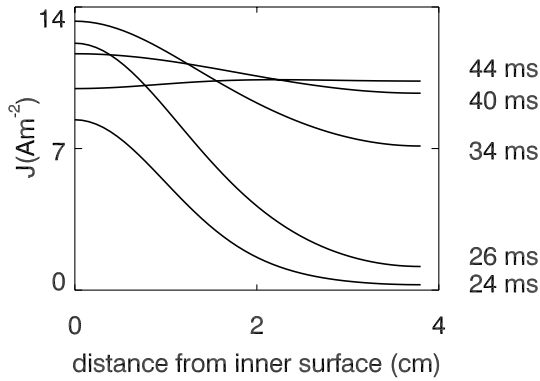


**Figure 5.** Computed radial profiles of the toroidal current in the vessel on the midplane for discharge 35345. (Note that the poloidal field currents are initialized at  $t = 21$  ms.)

shows that the induced current has diffused to the outer wall within 5 ms of current initialization. After  $t = 40$  ms  $B_z$  rises rapidly. At  $t = 34$  ms, at the time of peak current on the inner wall,  $J_{out}/J_{in} = 54\%$ , and between  $t = 40$  ms and  $t = 44$  ms the radial current profile is almost completely flat.

#### 4.2. Equilibrium reconstruction of a plasma discharge

START discharge 36429 serves to illustrate the equilibrium reconstruction process. This is an ohmic H mode discharge [28], and the reconstruction discussed here is made during the ELM phase at  $t = 41$  ms. This is 6 ms after neutral beam injection has ceased, by which time the energetic particles have thermalized. The time histories of the poloidal field coil currents displayed in Fig. 6 show that at  $t = 41$  ms the external vertical field is supplied by the  $B_V$  coils and that the current in the  $O_H$  coils has decayed to nearly zero. As shown in Fig. 6, this occurs during a quasi-steady-state period with  $I_p \approx 200$  kA. Measurements of line integrated density and SXR emission provide clear evidence of sawtooth activity from around 35 ms. At this time, radial profiles of  $T_e$  and  $n_e$  are available from Thomson scattering and  $T_i = 220$  eV on-axis (obtained from charge exchange measurements). In addition, the SXR emission indicates an inversion radius at around 41 cm, giving an approximate radius for the  $q = 1$  surface. The SXR profile also indicates that the magnetic axis has a radius  $R < 34.6$  cm.

Initially, EFIT was run at 1 ms intervals from  $t = 22$  ms, immediately following the flux compression phase, fitting the measured poloidal field cur-

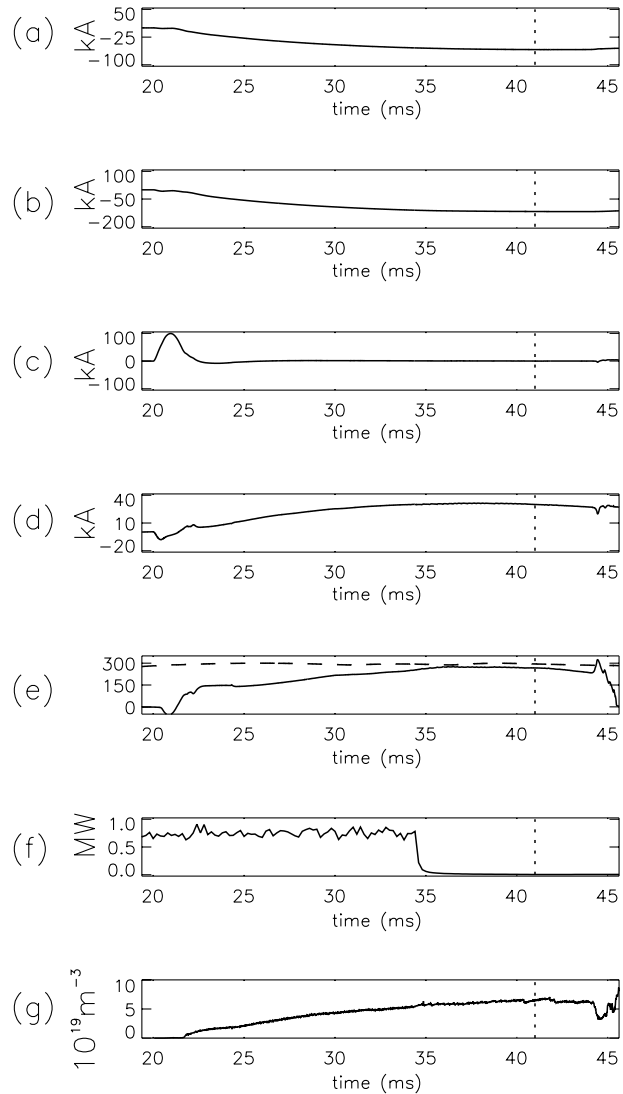


**Figure 6.** Details of START discharge 36429: (a) outer  $B_V$  coil current; (b) inner  $B_V$  coil current; (c)  $O_H$  coil current; (d) divertor coil current; (e) plasma current in kA, toroidal field at geometric axis in mT (dashed line); (f) neutral beam power; (g) line averaged density. The time ( $t = 41$  ms) at which Thomson scattering data were obtained is shown, when the discharge is dominated by ohmic heating.

rents, plasma current and magnetic detector signals to within 5%, with the flux values on the wall constrained to zero. Subsequent runs of EFIT were at  $t = 41$  ms with the flux at the wall constrained to within  $10 \mu\text{Wb}/\text{rad}$  of the values computed using Eq. (21) and other magnetic signals fitted to within 5% of measured values (the magnitude of these signals ranged between 80 and 350 mT). Figure 7 shows the variation of  $\beta_t = 2\mu_0\langle p \rangle / B_0^2$  with  $q$  at the magnetic axis (where  $\langle \dots \rangle$  denotes an average over the

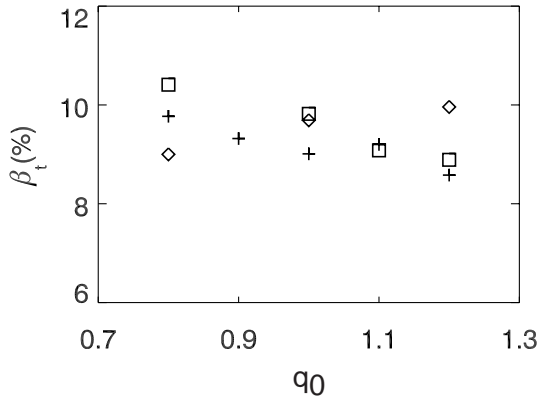


**Figure 7.** Results of EFIT reconstructions for discharge 36429 obtained using only the measured  $B_z$  signals on the centre column and measured coil currents. Plasma function representation is as follows: crosses,  $p' = a + b\bar{\psi}$ ,  $ff' = c + d\bar{\psi}_p$ ; squares,  $p' = a + b\bar{\psi}$ ,  $ff' = c$ ; diamonds,  $p' = a(1 - \bar{\psi}^2) + b(\bar{\psi} - \bar{\psi}^2)$ ,  $ff' = c(1 - \bar{\psi})$ . (Note that primes denote  $\partial/\partial\bar{\psi}$ ; in addition,  $\bar{\psi} = (\psi_p - \psi_0)/(\psi_b - \psi_0)$ .)

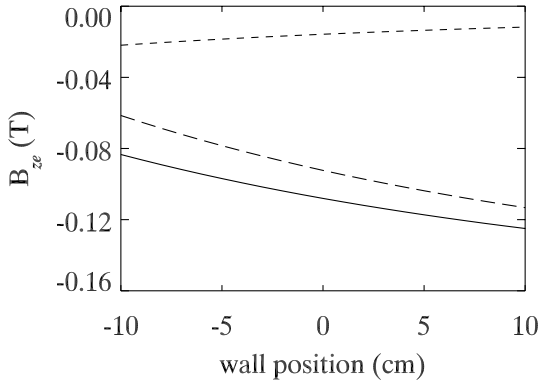


**Figure 8.** Calculated external magnetic field at  $R = 0.33$  m,  $Z = 0$  m as a function of the position of an ideal wall with respect to the inner surface of the actual resistive wall (solid curve). The contributions resulting from the poloidal field coil currents (long dashed curve) and plasma current (short dashed curve) are also shown.

plasma volume and  $B_0$  is the vacuum toroidal field evaluated at the geometric axis). The calculations were carried out with EFIT fitting only to the measured magnetic signals, coil and plasma currents and with the value of  $q$  at the magnetic axis constrained in the manner described in Ref. [5]. The results show that  $\beta_t \approx 9.5 \pm 1\%$  using several representations for the plasma flux functions  $p'$  and  $ff'$  (the precise representations are indicated in Fig. 7).

The effect of flux diffusion into the vessel on  $\beta_t$  can be estimated in the following way. The conduct-

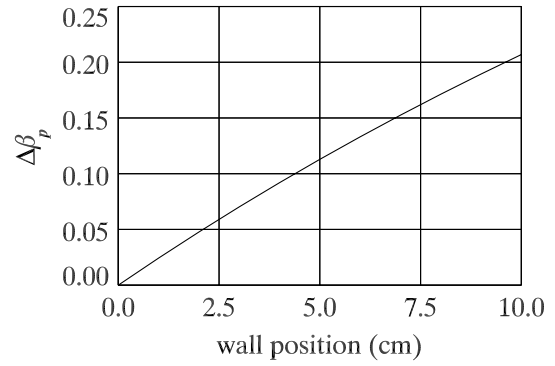


**Figure 9.** Calculated variation of  $\Delta\beta_p = \beta_p - \beta_{p(\text{inner})}$  as a function of the position of an ideal wall where  $\beta_{p(\text{inner})}$  is the value of  $\beta_p$  with the ideal wall located on the inner surface of the actual wall.

ing wall acts to modify the vertical field maintaining the radial force balance of the plasma. At large aspect ratio, the outward force of a plasma with minor radius  $a$ , major radius  $R$  and carrying current  $I_p$  is given by [29, 30]

$$F_p = \frac{\mu_0 I_p^2}{2} \left( \ln \frac{8R}{a} - \frac{3}{2} + \frac{l_i}{2} + \beta_p \right) \quad (22)$$

where  $\beta_p = 2\mu_0 \langle p \rangle / B_a^2$ ,  $B_a = \mu_0 I_p / (2\pi a)$  and  $l_i$  is the plasma internal inductance. This is balanced by a force due to the external field  $B_{ze}$  resulting from currents in the poloidal field coils and induced currents in the wall,

$$F_e = -2\pi B_{ze} I_p R. \quad (23)$$

Figure 8 shows a graph of  $B_{ze}$  at  $R = 0.33$  m,  $Z = 0$  m (the approximate location of the magnetic axis) with a flux conserving wall moved between +10 and -10 cm of the inner START wall position. The results were obtained with the poloidal field currents and plasma current measured at  $t = 41$  ms. The plasma current was represented with a single filament at  $R = 0.33$  m,  $Z = 0$  m. The total external field is made up of two components, that arising from the poloidal field coil currents and that arising from the plasma current. These are also plotted and show a competing effect with the contribution from the poloidal field coils increasing in magnitude as the wall is moved outwards whilst the contribution from the plasma current decreases. Equating (22) and (23), the variation of  $\beta_p$  with wall position can be obtained as shown in Fig. 9. Note that the result assumes invariance of  $R/a$  and  $l_i$ . For the experimental parameters, the effective skin depth on the vertical wall of START is (from Eq. (35))

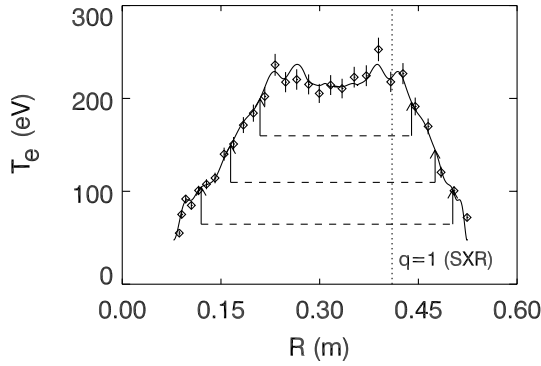


**Figure 10.** Radial  $T_e$  profile obtained from Thomson scattering for discharge 36429 (diamonds). The solid curve shows the mapped flux surface locations from the EFIT reconstructions. The long dashed lines show the locations of the relational constraints used to constrain EFIT and the short dashed line shows the location of the  $q = 1$  surface as inferred from the SXR measurements.

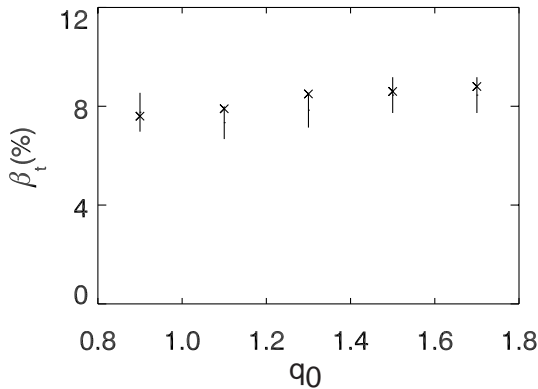


**Figure 11.** Results of EFIT reconstructions for discharge 36429 showing the variation of  $\beta_t$  with  $q_0$  when the inboard and outboard fluxes are constrained to be equal at three pairs of points, as shown in Fig. 10. The error bars of results obtained with 2% Gaussian noise applied to the magnetic data are superimposed.

$\delta$  (cm) =  $[1/(n + 1)]0.113t$  (ms) + 1.26, in which the tangential magnetic field  $B_s$  incident on the inner surface of the wall is assumed to vary as  $B_s \propto t^n$ . At  $t = 20$  ms,  $\delta \leq 3.5$  cm for  $n > 0$ . This is equivalent to an outward movement by a distance  $\delta$  of a flux-conserving wall. Thus, from Fig. 9, ignoring the effects of flux diffusion could result in an underestimate of  $\beta_p$  by  $\sim 0.08$ . Since in START the poloidal and toroidal fields are of the same magnitude, there will be a similar error on  $\beta_t$ .

Next, runs were carried out using the radial  $T_e$  profile to constrain the relative locations of poloidal

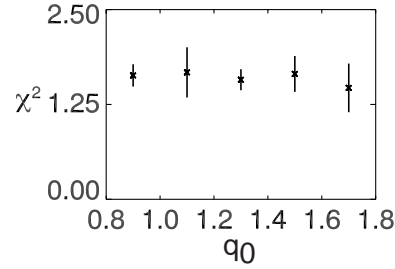


**Figure 12.** Results of EFIT reconstructions for discharge 36429 with 2% Gaussian noise applied to the magnetic data. The variation of  $\chi^2$  is plotted, showing its insensitivity to  $q_0$ .

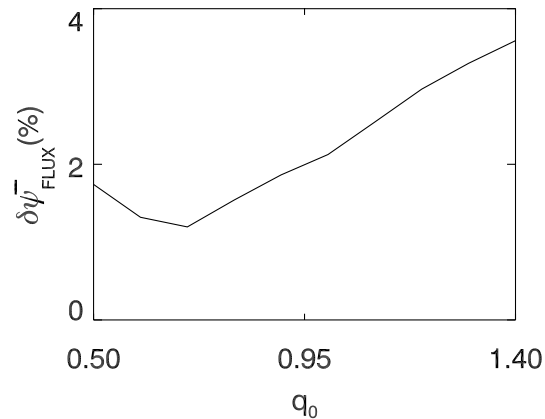


**Figure 13.** Result showing the discrepancy in poloidal flux values at the internal constraint locations for discharge 36429.

flux surfaces at three pairs of points on the midplane: (i)  $R = 12$  cm and  $R = 50.2$  cm; (ii)  $R = 16.5$  cm and  $R = 47.5$  cm; (iii)  $R = 21$  cm and  $R = 44$  cm. Figure 10 shows the measured  $T_e$  radial profile onto which are mapped flux surface locations. The steep  $T_e$  gradient close to the edge provides a strong constraint on the outer flux surfaces (and hence plasma volume) when the isoflux constraint is applied, but not on the inner surfaces in the range  $28 \text{ cm} \lesssim R \lesssim 40$  cm. Figure 11 indicates the variation of  $\beta_t$  with  $q_0$ . Error bars show the sensitivity to the results of applying 2% Gaussian noise to the magnetic data. These results were obtained using the following representation for the plasma functions:  $p' = \sum_{i=0}^{i=1} a_i \bar{\psi}^i$ ,  $ff' = \sum_{i=0}^{i=3} b_i \bar{\psi}^i$ . Within these error bounds, the predicted value of  $\beta_t$  is  $8 \pm 1\%$ , which is close to the range of values obtained above using no internal constraints, and it is insensitive to variations in  $q_0$ . In principle, the value of  $q_0$  can be deduced by finding the equilibrium solution which fits best to the data.

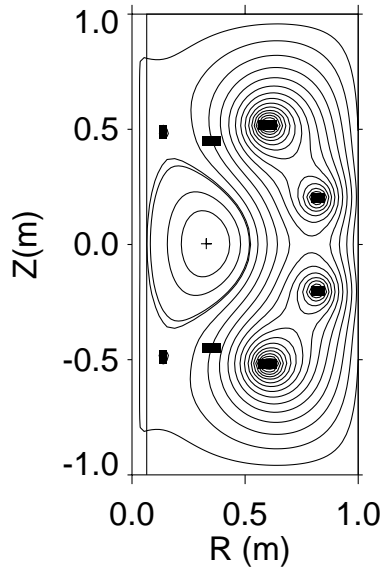


**Figure 14.** Reconstructed poloidal flux contours for discharge 36429.

Figure 12 shows the variation of  $\chi^2$  with  $q_0$ , where

$$\chi^2 = \frac{1}{N} \sum \left( \frac{M_i - P_i}{0.02M_i} \right)^2$$

in which  $M_i$  and  $P_i$  denote measured and predicted magnetic signals, respectively. The result indicates that  $q_0$  is insensitive to variations in  $\chi^2$ , which is in agreement with results reported previously [4]. Next, the sensitivity of  $q_0$  to discrepancies in the flux values between each of the three pairs of relational constraint locations is examined. Figure 13 shows a scan of the average flux discrepancy  $\delta\bar{\psi}_{FLUX}$  for  $0.5 < q_0 < 1.4$ . (The definition of  $\delta\bar{\psi}_{FLUX}$  is

$$\sqrt{\sum_{i=1}^3 \left( \bar{\psi}_1^{(i)} - \bar{\psi}_0^{(i)} \right)^2 / 3}$$

in which  $\bar{\psi}_0^{(i)}$  and  $\bar{\psi}_1^{(i)}$  are, respectively, inboard and outboard predicted values of poloidal flux for the  $i$ th relational constraint, normalized to 0 on the magnetic axis and to 1 on the separatrix.) The results, obtained in the absence of noise, indicate that a minimum in  $\delta\bar{\psi}_{FLUX}$  occurs around  $q_0=0.7$ . However, since the uncertainty in the position of constraint locations (as shown in Fig. 10) is at least 2 cm, the uncertainty in normalized poloidal flux will be significantly higher than 2%, and hence this value for  $q_0$  cannot be substantiated.

A poloidal cross-section of the solution with  $q_0 = 0.9$  is shown in Fig. 14. This value of axial  $q$  is reasonable since the discharge is sawtoothing at this

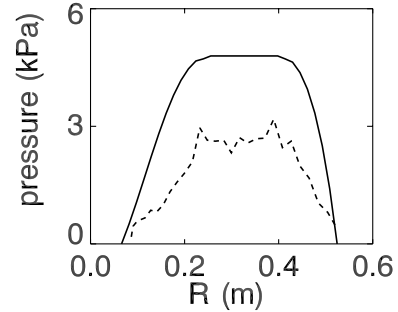


**Figure 15.** EFIT computed pressure profile on the mid-plane (solid line) and the electron pressure obtained from Thomson scattering (dashed line).

time. In addition, both the location of the outboard edge of the  $q = 1$  surface at  $R = 40.6$  cm and the position of the magnetic axis at  $R_{mag} = 32.7$  cm are consistent with the SXR data. Figure 15 shows the EFIT computed pressure profile and the measured electron pressure profile. Assuming the dominant impurity is carbon, and the ion and electron temperatures to be equal (this is indicated by the single charge exchange measurement), provides an estimate of effective charge  $Z_{eff}$  consistent with the measured total thermal pressure,

$$Z_{eff} = \frac{7p_e - 6p_i}{p_e} \simeq 2.$$

## 5. Discussion

The EFIT algorithm has been extended to enable the poloidal flux at multiple locations within the plasma to be constrained, to provide a robust method for including the radial profile of  $T_e$  obtained from Thomson scattering.

A model to account for flux diffusion through the START wall has been developed. The model is based on linear superpositions of solutions of the 1-D diffusion equation and is valid for times shorter than the resistive decay time of the wall. Calculations have shown that the effect of finite diffusion into the vessel could increase  $\beta_t$  by around 0.08 (i.e. 8%).

Reconstructions obtained using magnetic data and relational constraints between flux surfaces have demonstrated that  $\beta_t$  values can be obtained to within a fractional error of  $\pm 10\%$ . The fit to magnetic signals alone does not constrain  $q_0$ ; however, by including constraints on the internal flux surface locations, the principle of constraining  $q_0$  has been demonstrated. In the present instance the stringent accuracy of the requirements on the relational constraints means that they cannot be used to provide

information on the value of  $q_0$ . The use of only the poloidal flux contours in the confinement region and the total plasma current to fully define the equilibrium has been shown in previous work by Braams [31]. Expressions for the toroidal current density and  $q_0$  in terms of the elongation of flux surfaces valid at large aspect ratio [32] suggest that additional measurements relating the poloidal flux values in a vertical plane (e.g., from a vertical  $T_e$  vertical profile) may also be beneficial. However, the sensitivity of  $q_0$  to elongation of flux surfaces given in Ref. [32] suggests that additional measurements to constrain gradients in poloidal flux (i.e. poloidal magnetic field) are required to achieve accurate predictions on the  $q$  profile. In future work it is planned to address the effect that beam induced toroidal plasma rotation will have on the magnetic equilibrium.

## Appendix

### Analytical formulas for flux diffusion

Simple formulas for the effective skin depth defined in Eq. (14) as

$$\delta = \frac{\psi_p(x=0)}{G} \quad (24)$$

are given for the two regimes discussed in Section 3. For short timescales the wall appears to be infinitely thick. For long timescales the wall current is uniform across the wall and the flux gradient (i.e. the magnetic field) at the outer edge of the wall is small and can be taken to be zero, provided the timescale is less than  $t_L$  as given by Eq. (18).

A1. Short timescales:  $0 < t \lesssim 0.4\mu\sigma d^2$

A textbook solution for the poloidal flux at the surface of the wall (Ref. [25], p. 76) is

$$\psi_p(t) = \frac{1}{\sqrt{\pi\mu\sigma}} \int_0^t \frac{G(\tau)d\tau}{\sqrt{t-\tau}}. \quad (25)$$

If  $G(t) = 0$  for  $t < 0$ , and then has a power law variation  $G(t) \propto t^n$  for  $t > 0$

$$\delta(t) = C_n \sqrt{\frac{t}{\sigma\mu}} \quad (26)$$

where  $C_n$  is a number depending on the index  $n$  in the power law for  $G(t)$

$$C_n = \frac{\Gamma(n+1)}{\Gamma(n+3/2)} \quad (27)$$

**Table 1.** Values of  $C_n$ ,  $G(t)$  and  $\psi_p(x=0)$  for several values of  $n$

$n$	$C_n$	$G(t)$	$\psi_p(x=0)$
-1/2	$\sqrt{\pi} = 1.77$	$\propto 1/\sqrt{t}$	const.
0	$2/\sqrt{\pi} = 1.13$	const.	$\propto 1/\sqrt{t}$
1/2	$\sqrt{\pi}/2 = 0.885$	$\propto \sqrt{t}$	$\propto t$
1	$4/(3\sqrt{\pi}) = 0.75$	$\propto t$	$\propto t^{3/2}$

where  $\Gamma$  is the gamma function. Table 1 gives values of  $C_n$ ,  $G(t)$  and  $\psi_p(x=0)$  for particular values of  $n$

The case  $n = 0$  corresponds to Eq. (14). For large values of  $n$ , and even for these small ones,  $C_n$  is well approximated by the formula

$$C_n = \frac{1}{\sqrt{n+0.75}}. \quad (28)$$

A2. Long timescales:  $\sim \mu\sigma d^2 < t < t_L$

For times long compared with the short time constant  $\mu\sigma d^2$  (but short enough that external field leakage is still small), a formula for flux distribution in the wall can be found by assuming that the applied field  $G(t)$  varies slowly (i.e. varies by a small amount in a time  $\mu\sigma d^2$ ). The wall has filled up with flux, which is now leaking across into the outside region. The solution is essentially an expansion in the small parameter  $\mu\sigma d^2 \partial/\partial t$  and with the notation  $y = d-x$  takes the form

$$\begin{aligned} \psi_p(t, y) = & \frac{1}{\mu\sigma d} \int_0^t G(t) dt + dG(t) \left( \frac{y^2}{2d^2} - \frac{1}{6} \right) \\ & + \mu\sigma d^3 \frac{\partial G(t)}{\partial t} \left( \frac{y^4}{24d^4} - \frac{y^2}{12d^2} + \frac{7}{360} \right) + \dots \end{aligned} \quad (29)$$

The poloidal field component tangential to the wall at radius  $R$  is

$$B_p(t, y) = \frac{yG(t)}{Rd} + \frac{\mu\sigma d^2}{6R} \frac{\partial G(t)}{\partial t} \left( \frac{y^3}{d^3} - \frac{y}{d} \right) + \dots \quad (30)$$

and the current density follows from substituting Eq. (29) for  $\psi_p$  into Eq. (12),

$$\begin{aligned} J(t, y) = & \frac{1}{\mu} \frac{\partial B_p(t, y)}{\partial y} \\ = & \frac{G(t)}{R\mu d} + \frac{\sigma d}{R} \frac{\partial G(t)}{\partial t} \left( \frac{y^2}{2d^2} - \frac{1}{6} \right) + \dots \end{aligned} \quad (31)$$

These solutions show that, to the lowest order, the field distribution  $B_p(t, y)$  falls linearly from the wall

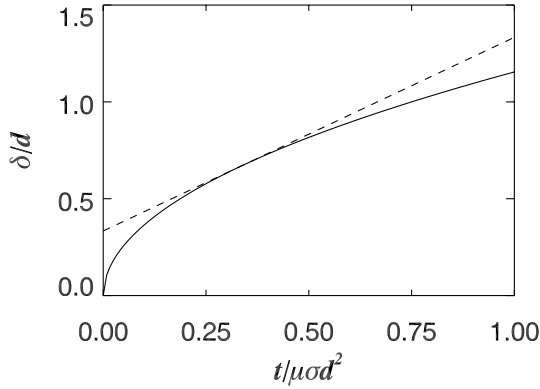


**Figure 16.** Time variation of skin depth for  $n = 0$  for short timescales (solid curve) and longer timescales (dashed curve). With this choice of  $n$ , the curves touch at  $t/\mu\sigma d^2 = 1/3$ .

value  $G(t)$  inside to zero outside and the current distribution is uniform, as it would be in a steady state layer. Since the boundary conditions are that  $B_p$  is given at  $y = 0$  and  $y = d$ , the values of  $B_p$  in the perturbation terms are zero at  $y = 0$  and  $y = d$ , and the corresponding time variation in total current  $\int J(t, y) dy = 0$  although the spatial variation of  $J(t, y)$  is non-uniform. This gives rise to the following results for the flux on the walls:

$$\psi_p(t, d) = \frac{1}{\mu\sigma d} \int_0^t G(t) dt + \frac{dG(t)}{3} \quad (32)$$

$$\psi_p(t, 0) = \frac{1}{\mu\sigma d} \int_0^t G(t) dt - \frac{dG(t)}{6} \quad (33)$$

or for the effective skin depth (substituting Eq. (32) into (24))

$$\delta = \frac{1}{G(t)\mu\sigma d} \int_0^t G(t) dt + \frac{d}{3}. \quad (34)$$

The first term in these expressions is essentially the time integral of the electric field  $E = j/\sigma = G(t)/(R\mu\sigma d)$  required to drive a uniform current in the wall. Compared with an infinitely thin wall ( $d \rightarrow 0$ , but  $\sigma d$  kept fixed) the extra flux leakage is as though the wall has moved out by a distance  $d/3$ , not  $d/2$ , as one might have suspected. The factor  $1/3$  is for the case of zero  $B$  outside and depends in general on the ratio of  $B$  at the inner and outer surfaces.

The formula for the effective skin depth when  $\delta(t) \propto t^n$  in this long timescale regime, corresponding to Eq. (26) in the short timescale regime, is

$$\delta(t) = \frac{t}{(n+1)\mu\sigma d} + \frac{d}{3}. \quad (35)$$

For intermediate times  $0.4 < t/\mu\sigma d^2 < 1$ , the skin depth can be estimated by interpolation between the two formulas. The time dependence for the case  $n = 0$  is shown in Fig. 16.

## Acknowledgements

The work was jointly funded by the UK Department of Trade and Industry and Euratom. The authors would like to thank L. Lao for providing the EFIT code and for useful discussion. They are also grateful to R. Martin, N. Conway, I. Jenkins and the START team for providing the experimental data.

## References

- [1] Shafranov, V.D., Sov. Phys. – JETP **37** (1960) 775.
- [2] Mukhovatov, V.S., Shafranov, V.D., Nucl. Fusion **11** (1971) 605.
- [3] Shafranov, V.D., Plasma Phys. **13** (1971) 757.
- [4] Luxon, J.B., Brown, B.B., Nucl. Fusion **22** (1982) 813.
- [5] Lao, L.L., St. John, H., Stambaugh, R.D., Kellman, A.G., Pfeiffer, W., Nucl. Fusion **25** (1985) 1611.
- [6] Alladio, F., Crisanti, F., Nucl. Fusion **26** (1986) 1143.
- [7] Braams, B.J., Jilge, W., Lackner, K., Nucl. Fusion **26** (1986) 699.
- [8] Kuznetsov, Yu.K., Pyatov, V.N., Yasin, I.V., Sov. J. Plasma Phys. **13** (1987) 75.
- [9] Hofmann, F., Tonetti, G., Nucl. Fusion **28** (1988) 1871.
- [10] Blum, J., Lazzaro, E., O'Rourke, J., Keegan, B., Stephan, Y., Nucl. Fusion **30** (1990) 1475.
- [11] Alladio, F., Micozzi, P., Nucl. Fusion **35** (1995) 305.
- [12] Alladio, F., Micozzi, P., Nucl. Fusion **37** (1997) 1759.
- [13] Cooper, W.A., Wootton, A.J., Plasma Phys. **24** (1982) 1183.
- [14] Salberta, E.R., Grimm, R.C., Johnson, J.L., Manickam, J., Tang, W.M., Phys. Fluids **30** (1987) 2796.
- [15] Iacono, R., Bondeson, A., Troyon, F., Gruber, R., Phys. Fluids B **2** (1990) 1794.
- [16] Morse, P., Feshbach, H., Methods of Theoretical Physics, McGraw-Hill, New York (1953).
- [17] Lao, L.L., et al., Nucl. Fusion **30** (1990) 1035.
- [18] O'Brien, D.P., et al., Nucl. Fusion, **32** (1992) 1351.
- [19] Sykes, A., et al., Nucl. Fusion **32** (1992) 694.
- [20] Lao, L.L., et al., Nucl. Fusion **25** (1985) 1421.
- [21] Walsh, M.J., Conway, N.J., Dunstan, M., Forrest, M.J., Huxford, R.B., Rev. Sci. Instrum. **70** (1999) 742.
- [22] Conway, N.J., Carolan, P.G., Tournianski, M.R., Rev. Sci. Instrum. **70** (1999) 934.

- [23] Cline, A.K., Commun. Assoc. Computing Machinery **17** (1974) 218.
- [24] Press, W., Flannery, B.P., Teukolsky, S.A., Vetterling, W.T., Numerical Recipes, Cambridge University Press, Cambridge (1989).
- [25] Carslaw, C.J., Jaeger, J.C., Conduction of Heat in Solids, 2nd edn, Oxford University Press, Oxford (1959).
- [26] Jackson, J., Classical Electrodynamics, Wiley, New York (1975).
- [27] Akers, R., et al., submitted to Nucl. Fusion.
- [28] Sykes, A., et al., Phys. Rev. Lett. **84** (2000) 495.
- [29] Shafranov, V.D., in Reviews of Plasma Physics, Vol. 2, Consultants Bureau, New York (1966).
- [30] Bateman, G., MHD Instabilities, MIT Press, Cambridge, MA (1978).
- [31] Braams, B.J., Rep. IPP5/2, Max-Planck-Institut für Plasmaphysik, Garching (1985).
- [32] Christiansen, J.P., Callen, J.D., Ellis, J.J., Nucl. Fusion **29** (1989) 703.

(Manuscript received 16 June 2000)

Final manuscript accepted 6 November 2000)

E-mail address of L.C. Appel:

lynton.appel@ukaea.org.uk

Subject classification: C0, Tm